ISSN 0030-400X, Optics and Spectroscopy, 2018, Vol. 125, No. 6, pp. 982–996. © Pleiades Publishing, Ltd., 2018.

NONLINEAR OPTICS

Strong Third-order Optical Nonlinearities of the Ag, Ni, Ti, and Co Nanoparticles Synthesized During Laser Ablation of Bulk Metals in Liquids[1]

R. A. Ganeev*

The Guo China-US Photonics Laboratory, State Key Laboratory of Applied Optics, Changchun Institute of Optics, Fine Mechanics and Physics, Chinese Academy of Sciences, Changchun, 130033 China

**e-mail: rashid_ganeev@mail.ru*

Received October 29, 2018

Abstract—Laser ablation of the materials immersed in liquid environment has been established as an advanced method for formation of the stable nanoparticles, especially those which cannot be synthesized by chemical methods. We review the studies of four metal (Ag, Ti, Co, Ni) nanoparticles synthesized during laser ablation in different liquids. The correlation between strong nonlinear optical response of silver nanoparticles out of plasmon resonance and efficient third harmonic generation in the plasmas containing silver nanoparticles is discussed. The change of sign of the nonlinear refraction with variation of the wavelength and duration of probe laser pulses is analyzed. The studies of third-order nonlinear optical processes (saturable absorption, reverse saturable absorption, two-photon absorption and nonlinear refraction) in the titanium and cobalt nanoparticles synthesized by laser ablation of bulk materials in water, toluene and ethylene glycol are discussed. The concurrence of different nonlinear absorption processes in nanoparticle-containing suspensions is analyzed. We discuss the two-photon absorption and nonlinear refraction studies of the nickel nanoparticles in water using femtosecond laser pulses at 400 and 800 nm. Third harmonic generation from the Ni nanoparticles contained plasma using picosecond and femtosecond pulses as heating radiation and femtosecond probe pulses is analyzed.

DOI: 10.1134/S0030400X18070275

1. INTRODUCTION

The synthesis of nanostructured materials took much attention due to their advanced optical and nonlinear optical properties, which can be used in various areas of communications, optics, laser physics and medicine. The attractive application of these nanostructured materials in optics is the protection of sensitive area of detection systems through optical limiting (OL) of high-power laser radiation. One can anticipate that variations of the sizes of nanoparticles (NPs) can significantly enhance OL. In [1], the metal NPs-embedded polymer films and their OL capability were demonstrated. Optical limiting behavior of silver NPs with different sizes and shapes is investigated and compared to the OL performance of conventional carbon black suspension [2]. It found that the OL is strongly particle size dependent and the best performance is achieved with the smaller particles.

The vast amount of research work has been carried out for demonstration of the large nonlinear optical response from NPs [3–6], which includes the two-photon absorption (2PA) and nonlinear refraction (NLR). Various procedures such as vapor phase synthesis, thermal evaporation, electrochemical synthesis and chemical reduction synthesis have been used for preparation and studies of NPs [7]. These preparation techniques do not apply efficiently to magnetic NPs such as iron, cobalt, nickel and titanium, whose metal ions are difficult to reduce for the formation of NPs due to their instability over the time.

The majority of laser ablation studies have been aimed on the formation of various NPs by focusing the laser pulses on the metal targets immersed in liquids [8–12]. Due to the resonance effect arising from the plasmon resonances of some NPs their size and shape can be controlled by laser irradiation in various solvents [13]. Advantages of this method are the high purity of the NPs, variety of materials, and the in situ dispersion of NPs in different liquids tolerating safe and stable control of the colloids [14, 15]. Additionally, the solvent molecules surrounding NPs can protect them in some cases from aggregation due to their viscosity and other properties. These studies have also shown the crucial influence of the wavelength and pulse duration of laser radiation on the size and shape of produced NPs [16].

[1] The article is published in the original.

Silver NPs took special attention among numerous small-sized species due to their use in imaging, biosensors, photovoltaic devices, solar cells, light emitting devices, catalysis, etc. They have unique optical, electrical, and thermal properties and are already found applications being incorporated into products that range from photovoltaics to biological and chemical sensors. Examples include conductive inks, pastes and fillers which utilize Ag NPs for their high electrical conductivity, stability, and low sintering temperatures. Additional applications include molecular diagnostics and photonic devices, which take advantage of the novel optical properties of these nanomaterials. Ag NPs are extraordinarily efficient at absorbing and scattering light and, unlike many dyes and pigments, have a color that depends upon the size and the shape of the particle. The strong interaction of the Ag NPs with light occurs because the conduction electrons on the metal surface undergo a collective oscillation when excited by light at specific wavelengths. The advantages of Ag NPs include monodisperse distribution in surrounding environment without agglomeration and aggregation, comprehensive characterization including TEM and UV-Vis, good stability and long life time. A unique property of spherical Ag NPs is that its surface plasmon resonance (SPR) can be tuned from 400 to 530 nm by changing the particle size and the local refractive index near the particle surface. Even larger shifts of resonance peak towards the IR region can be achieved by producing silver NPs with rod or plate shapes.

The titanium and cobalt small-sized species have also attracted the interest due to their various potential applications [17]. Titanium is not only a strong and light-weight metal, but also the one which is highly resistant to corrosion. Therefore, it is often used in aerospace and military applications. Ti NPs allow improvement of the radiation resistance. Ti NPs are used in different industrial applications, disease diagnostics, medical imaging and other fields [18]. They have high transparency in the visible range and high UV absorption. Co NPs found the applications in medical sensors, coatings, plastics, nanofibers, nanowires, textiles, and high-performance magnetic recording materials. Cobalt oxide NPs can also be used in military applications due to their strong absorption of visible, IR, and millimeter waves. Both Ti and Co are transition metals from the fourth period. Elements in the same period show trends in atomic radius, ionization energy, electron affinity, and electronegativity. Moving left to right across a period, atomic radius usually decreases. This decrease in atomic radius also causes the ionization energy to increase. Ti and Co have comparable boiling (3287 and 2927°C) and melting (1660 and 1495°C) temperatures, while different densities (4.54 and 8.9 g/cm^3). Their main thermal properties are similar. Apart from the above mentioned interest to Ti and Co NPs the search of peculiarities in the nonlinear optical response can give additional information about their structural properties and potential applications.

The studies of magnetic NPs were mostly concentrated on Fe, Ti, Co and their respective composite materials [19, 20]. This eventually led to the lack of information about optoelectronic properties of Ni NPs including their nonlinear optical parameters. Meanwhile, Ni NPs have attracted considerable interest due to their ferromagnetic properties [21, 22], which can also modify their nonlinear optical characteristics. Most of the studies on Ni NPs have been carried out in their oxidized form or in composite materials [23, 24]. There are few reports on the laser ablation of Ni in liquids using long laser pulses [25, 26]. The only study on the nonlinear optical response of Ni NPs is presented in [27] where self-defocusing due to the thermo-optical properties and thermal heating effect have been shown. However, the electronic nonlinear optical response from Ni NPs induced by short pulses has not been reported so far, which promoted researchers to study these properties of Ni NPs under the influence of femtosecond laser excitation.

The laser ablation in liquids is not the only technique used for preparation of NPs. Ni plasma formation in air can serve, particularly, as a nonlinear medium for harmonic generation in the plasma containing NPs. Earlier, the harmonic generation in plasma has been performed at vacuum conditions. The plasma created during laser ablation contains electrons, atoms and molecules, ions, neutrals, clusters, quantum dots and NPs. The synthesis of NPs during plasma formation in ablation plume has been shown to significantly influence the efficiency of high-order harmonic generation (HHG). At the same time, Ni NPs have been applied to study the low-order harmonic generation in microcube structures [28].

The low-order nonlinearities of NPs, which are responsible for third harmonic generation (THG) in laser-produced plasmas (LPP), were studied in [29]. The LPPs are also considered as the attractive nonlinear media for conversion of the frequency of ultrashort infrared laser pulses towards the ultraviolet and extreme ultraviolet (XUV) ranges [30]. The advantages of using in situ produced Ag NPs for HHG due to large nonlinear optical response of Ag NPs in the field of femtosecond probe pulses were analyzed in [31]. The spectral characteristics of harmonics from NPs produced in situ were compared with the HHG from preformed NPs-containing plasma.

In this review, we summarize the low-order nonlinear optical properties of four metal NPs (Ag, Ni, Ti, and Co). We discuss the systematic studies of the ablation-produced Ag NPs prepared by 5 ns, 200 ps, and 60 fs pulses at the wavelengths of 1064 and 800 nm. We analyze the OL in Ag NP suspension induced by 2PA and reverse saturable absorption (RSA) at the wavelengths of 800 and 355 nm, respectively. Third harmonic generation in the plasmas containing Ag NPs is

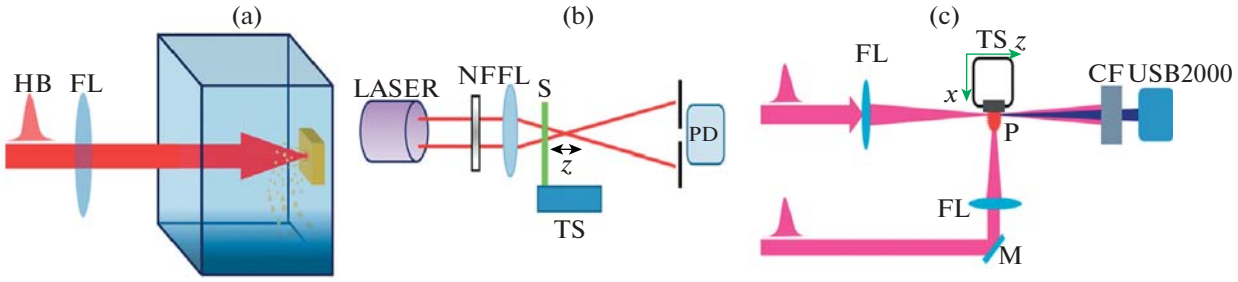

Fig. 1. (Color online) (a) Experimental setup for laser ablation in liquid. HB: heating beam, FL: focusing lens. (b) Experimental setup for *Z*-scan studies. LASER: Q-smart 850 nanosecond laser or Ti:sapphire femtosecond laser, NF: neutral filters, FL: focusing lens, S: sample, TS: translating stage, PD: photodiode. (c) Experimental scheme for third harmonic generation in laser plasma. FL: focusing lenses, M: mirror, VC: vacuum chamber, TS: translating stage, T: target, P: plasma, CF: color filters, FS: fiber spectrometer (USB2000). Reproduced from [32]. With permission of Springer.

discussed. The correlation between strong nonlinear optical response of silver NPs out of their SPR and efficient THG in the plasmas containing Ag NPs is analyzed. Further, the studies of the nonlinear optical properties of Ni NPs prepared using laser ablation in deionized water and air are discussed. The determination of the 2PA coefficients and NLR indices under femtosecond excitation at 800 nm and 400 nm is described. We also discuss the THG in Ni plasma in ambient air using picosecond and femtosecond heating pulses. Finally, we analyze the ablation using picosecond laser pulses and formation of Ti and Co NPs in three liquids. Three solvents (water, toluene, and ethylene glycol (EG)) were used during ablation to create the NPs of Ti and Co and control their sizes and shapes. It was observed that the size and shape of NPs vary in different surrounding liquids at similar laser ablation conditions. We discuss the results of measurements of the nonlinear refractive indices, nonlinear absorption coefficients, and saturated intensities of these NPs at the wavelengths of 800 and 400 nm (at pulse duration of $t = 60$ fs), as well as 355 nm ($t = 5$ ns). We also analyze the OL studies in the suspensions containing these NPs.

2. STRONG THIRD-ORDER OPTICAL NONLINEARITIES OF Ag NPs SYNTHESIZED BY LASER ABLATION OF BULK SILVER IN WATER AND AIR

The Ag NPs were synthesized by ablation of bulk silver in water using nanosecond laser (Q-Smart 850, Coherent) [32]. Laser radiation (wavelength: 1064 nm, pulse duration: 5 ns, pulse repetition rate: 10 Hz, pulse energy: 40 mJ) was focused by the 100 mm focal length lens on the surface of silver target immersed in deionized water [Fig. 1a]. The target sizes was $5 \times 5 \times 2$ mm. The silver target was moved by two-coordinate translating stage during laser ablation. The ablation was carried out during 30 min. The color of suspension was changed during laser ablation until became yellow shade. The silver target was also ablated using 200 ps, 800 nm and 60 fs, 800 nm laser pulses.

The nonlinear optical parameters of Ag NP suspension were investigated using *Z*-scan technique. The nonlinear optical studies of Ag NP suspensions were carried out using nanosecond and femtosecond laser pulses at four different wavelengths (1064, 800, 400 and 355 nm). The closed-aperture (CA) and the open-aperture (OA) *Z*-scan schemes were used for nonlinear optical characterization of studied samples. The radiation of Nd:YAG laser ($\lambda = 1064$ nm, $\tau = 5$ ns) or its third harmonic ($\lambda = 355$ nm) was focused by a 200 mm focal length lens (Fig. 1b). The beam waist diameters were 81 and 39 μm (at $1/e^2$ level of the spatial distribution at the focal plane) in the case of fundamental and third harmonic radiation, respectively. The propagated pulses were detected by a large aperture photodiode.

The 2-mm-thick fused silica cell containing Ag NP suspension was moved along the *z*-axis through the focal point using a translating stage. The maximal used intensities of probe radiation in the experiments did not exceed 1.6×10^9 ($\lambda = 1064$ nm) and 6×10^8 W cm^{-2} ($\lambda = 355$ nm). The Ti:sapphire laser (Spitfire Ace, Spectra Physics) provided 60 fs, 800 nm or 210 ps, 800 nm pulses at 1 kHz pulse repetition rate. The intensities of used femtosecond pulses ($\tau = 60$ fs) did not exceed 2×10^{10} ($\lambda = 800$ nm) and 1.6×10^{10} W cm^{-2} ($\lambda = 400$ nm). The stability of morphology was controlled by analyzing the position of SPR, which was not changed during three months. Additionally, TEM and SEM studies confirmed the conclusion about good stability of synthesized NPs.

In the case of THG studies the laser radiation ($\lambda = 800$ nm, $\tau = 60$ fs) was focused by a 400 mm focal length lens on the LPP (Fig. 1c). The spectral characteristics of third harmonic radiation ($\lambda = 266$ nm) were analyzed by a fiber spectrometer. To create plasma plume, a pulse was split from the Ti:sapphire laser by a beamsplitter before the compression of fundamental uncompressed pulse. The heating pulse duration was

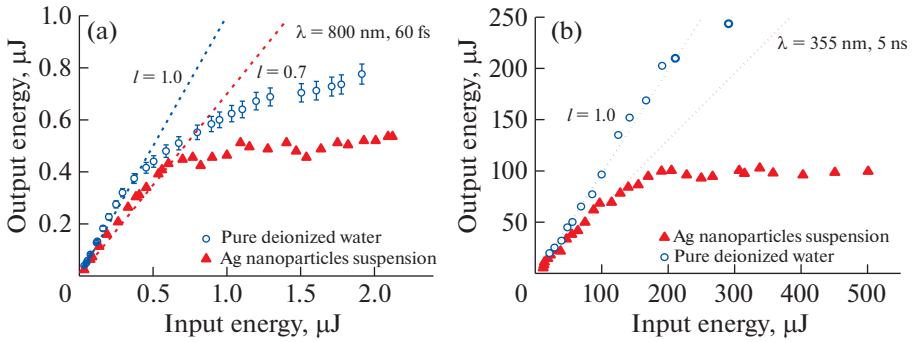

Fig. 2. (Color online) Optical limiting in the aqueous suspension of Ag NPs (filled triangles) and pure water (empty circles) using (a) 60 fs, 800 nm, and (b) 5 ns, 355 nm probe pulses. Dotted lines show the linear dependences between output and input pulse energies at the lower energy ranges of input pulses. Reproduced from [32]. With permission of Springer.

210 ps. This radiation was focused on the target to heat it and produce LPP in the air conditions (Fig. 1c). The area of ablation was adjusted to be approximately 0.25 mm. A delay between fundamental and heating pulses was maintained to be 38 ns.

2.1. Optical Limiting in Ag NP Suspension

Below, the OL studies using the 800 nm, 60 fs and 355 nm, 5 ns laser pulses, which propagated through the suspension of Ag NPs in deionized water, are presented. The suspension was obtained during ablation of bulk silver using nanosecond laser pulses. This suspension was placed at the focal plane of 400 mm focal length lens.

The linear dependence between input and output 800 nm, 60 fs pulses was maintained up to the input pulse energy of ~0.6 μJ (Fig. 2a, filled triangles). Further growth of input pulse energy led to OL of propagated laser radiation due to 2PA. This process was maintained up to the energy of 800 nm pulses of ~2.0 μJ, which allowed stabilization of output energy at the level of 0.5 μJ along the 0.6–2.2 μJ energy range of input pulses. The OL in pure water was also studied in this energy range of propagated laser pulses. The slope of linear fitting for pure deionized water at small input pulse energies was equal to 1.0, while the slope of linear fitting of Ag NPs was equal to 0.7. The latter slope was corresponded to the initial transmittance of the suspension containing Ag NPs in deionized water. In the case of water the inclination of I_{out}/I_{in} from the linear dependence was also observed due to white light generation (Fig. 2a, empty circles).

In the case of nanosecond laser pulses, RSA led to the OL of 355 nm laser radiation. This process was analyzed in the range of energies between 150 to 600 μJ (Fig. 2b). One can see that Ag NP suspension demonstrated excellent OL properties in the case of nanosecond UV pulses. The observations of the OL in Ag NP suspension were attributed to 2PA and RSA at the wavelengths of 800 and 355 nm probe pulses, respectively.

2.2. Nonlinear Refraction and Absorption in Ag NPs Suspensions in the Case of IR and UV Laser Pulses of Different Duration

The dependences of refractive indices and absorption coefficients of materials on the laser intensity are presented as [33]

$$n = n_0 + \gamma I, \quad \alpha = \alpha_0 + \beta I. \tag{1}$$

Here n_0 is the linear refractive index, I is the intensity of laser beam, γ and β are the nonlinear refractive index and nonlinear absorption coefficient of media, and α_0 is the linear absorption coefficient. The determination of γ and β of materials can be accomplished using the analysis of Z-scan curves. The Z-scan curves in the cases of CA and OA schemes for the bulk silver ablated in deionized water using nanosecond and picosecond pulses are shown in Fig. 3. Circles and squares represent the experimental data and solid lines are the theoretical fits. In case of CA Z-scan scheme the normalized transmittance $T(z)$ is related to the nonlinear refractive index by

$$T(z) = 1 + 4\Delta\Phi_0 x/(x^2 + 1)(x^2 + 9). \tag{2}$$

Here $x = z/z_0$, $z_0 = 0.5kw_o^2$ is the Rayleigh length, $k = 2\pi/\lambda$ is the wave number, w_o is the beam waist radius of the focused beam and $\Delta\Phi_0$ is the phase change. The nonlinear refractive index is related to the phase change as $\gamma = \Delta\Phi_0/kL_{ef}I_0$, where $L_{ef} = [1 - \exp(-\alpha_0 L)]/\alpha_0$ is the effective length of nonlinear medium, I_0 is the intensity of laser beam at the focal plane of focusing lens, and L is the sample thickness. The normalized transmittance curves were fitted with the CA experimental data. In the case of OA Z-scans, the photodetector measured the whole transmittance of propagated radiation. Figure 3a–3d show the 2PA-induced OA Z-scans (empty circles). In that case

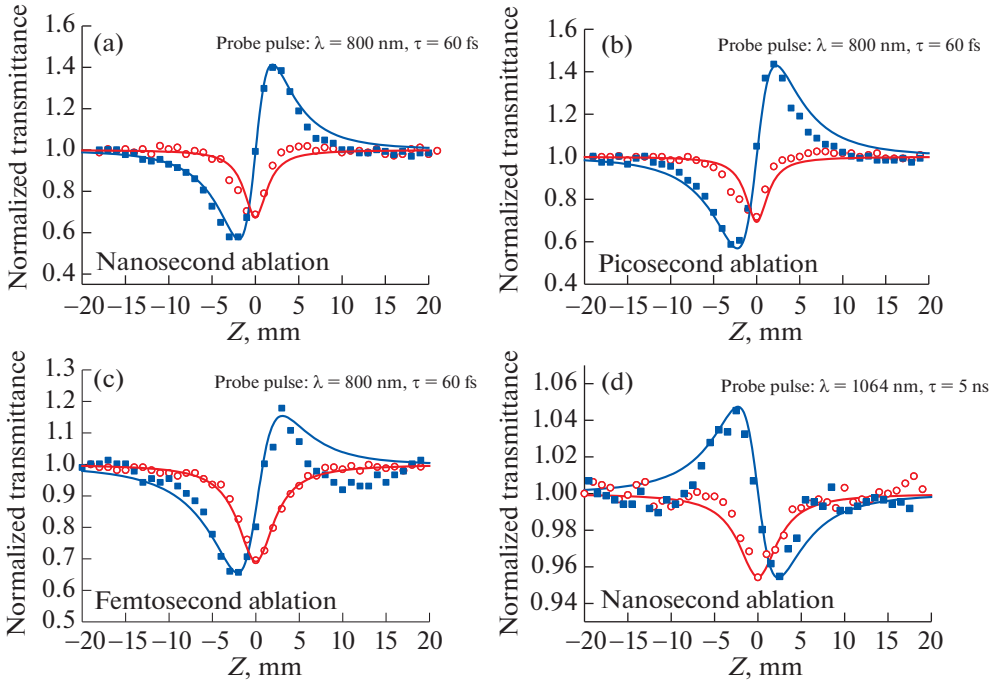

Fig. 3. (Color online) OA and CA *Z*-scans of Ag NP suspensions prepared by laser ablation of solid target using (a) 5 ns, 1064 nm, (b) 200 ps, 800 nm, and (c) 60 fs, 800 nm laser pulses. 60 fs, 800 nm pulses were used as a probe radiation in the (a), (b), and (c) cases. (d) OA and CA curves in the case of 5 ns, 1064 nm probe pulses. Ag NPs were prepared using 5 ns, 1064 nm pulses. Solid curves are the fits to experimental data (see text). Reproduced from [32]. With permission of Springer.

the normalized transmittance of laser pulses can be described by

$$T(z) \approx 1 - q_0/2\sqrt{2}. \quad (3)$$

Here, $q_0(z) = I_0\beta L_{ef}/[1 + z^2/(z_0)^2]$. Equation (3) was fitted with the OA data presented in Fig. 3.

The nonlinear optical parameters were studied in the field of nanosecond and femtosecond laser pulses. The thermal induced self-defocusing was observed in the case of 1064 nm, 5 ns probe pulses (Fig. 3d, filled squares). The reverse process was observed in the case of 800 nm, 60 fs pulses at 1 kHz repetition rate (Fig. 3a–3c, filled squares). This regime of interaction of femtosecond laser pulses with Ag NP suspension led to self-focusing, which is due to the electronic response of nanoparticles. The corresponding nonlinear optical parameters of 8 nm sizes Ag NPs in the case of 1064 nm, 5 ns probe laser pulses were: $\beta_{2PA} = 3.0 \times 10^{-10}$ cm W^{-1}, and $\gamma = 1.2 \times 10^{-14}$ cm^2 W^{-1}. At 800 nm, 60 fs probe pulses $\beta_{2PA} = 1.0 \times 10^{-10}$ cm W^{-1}, and $\gamma = 2.0 \times 10^{-15}$ cm^2 W^{-1}.

The Kerr-induced mechanism of self-defocusing for analysis of colloidal silver in the field of picosecond pulses has been considered in [34]. The thermal-induced effects can dominate over the fast Kerr-induced electronic contribution when the probe pulse duration becomes longer than the thermal conductivity relaxation time of small sized Ag NPs. Hence, the duration of laser pulses is a critical parameter for the evaluation of third-order nonlinear response, especially nonlinear refraction.

The dependences of OA and CA normalized transmittances of Ag NP suspensions at the wavelength of 400 nm femtosecond laser pulses are shown in Fig. 4. The 2PA, RSA, and saturable absorption (SA) parameters of used suspension at this wavelength were calculated by fitting the experimental data with the Eq. (3) and the relation describing SA:

$$T_{SA}(z) = 1 + \frac{I_o}{I_{sat}(x^2 + 1)}, \quad (4)$$

where I_{sat} is the saturated intensity of the medium.

Figure 4a demonstrates three processes: SA, RSA and self-focusing in silver NPs suspension at 400 nm, 60 fs probe pulses. These studies showed the dominance of the self-focusing process at higher energies of probe pulses. These data were fitted using the equation for three processes: SA, RSA and self-focusing.

The results of similar OA studies of Ag NP suspension ablated by nanosecond radiation using 355 nm, 5 ns probe pulses are shown in Fig. 5a. The corresponding nonlinear absorption coefficients of the studied samples at $\lambda = 355$ nm were as: $\beta_{SA} = -3 \times 10^{-11}$ cm W^{-1}, and $\beta_{RSA} = 2 \times 10^{-10}$ cm W^{-1}.

Figure 5b shows self-defocusing and 2PA of 355 nm laser radiation in Ag NP suspension ablated by picosecond laser pulses. The nonlinear optical param-

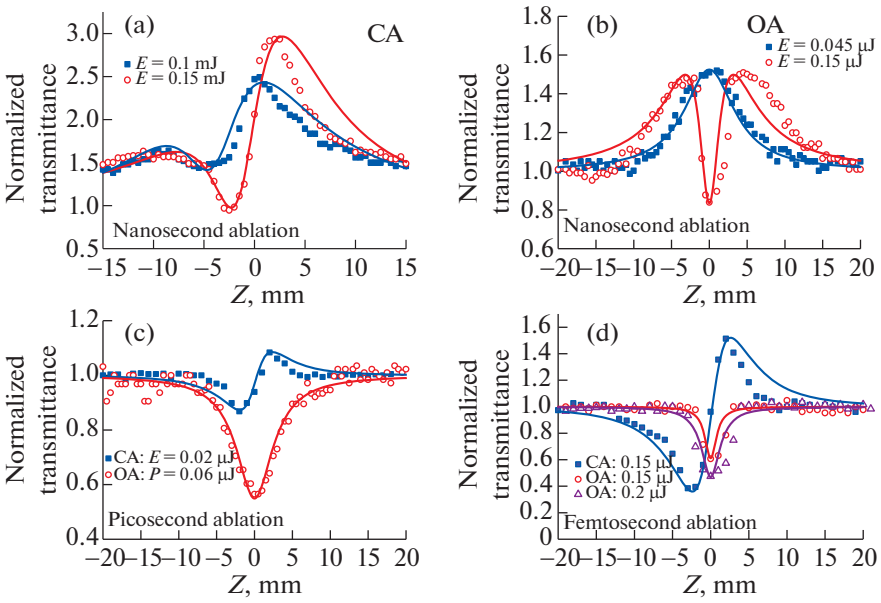

Fig. 4. (Color online) Measurements using 400 nm, 60 fs pulses. (a) CA and (b) OA *Z*-scans of the Ag NP suspension produced by 5 ns, 1064 nm pulses at different energies of probe pulses. (c) OA and CA *Z*-scans of the Ag NP suspension produced by 200 ps, 800 nm pulses. (d) OA and CA *Z*-scans of the Ag NP suspension produced by 60 fs, 800 nm pulses. Reproduced from [32]. With permission of Springer.

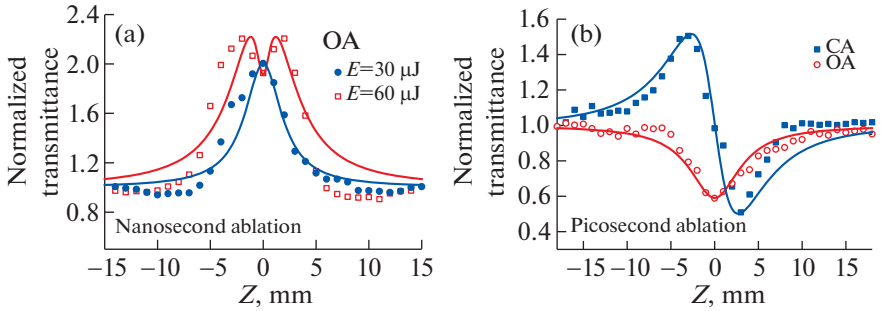

Fig. 5. (Color online) (a) SA and RSA in Ag NP suspensions prepared by ablation using nanosecond pulses at different energies of 355 nm, 5 ns probe pulses: (filled circles) 30 μJ and (empty squares) 60 μJ. (b) Self-defocusing and 2PA using 355 nm, 5 ns laser pulses ($E = 50$ μJ) in the case of the suspension prepared by picosecond pulses. Reproduced from [32]. With permission of Springer.

eters of the Ag NP suspensions measured at different experimental conditions are collected in Table 1. Notice that concentration of Ag NPs in the case of femtosecond ablation was notably smaller than concentration of the NPs produced during ablation using picosecond and nanosecond pulses due to less efficient ablation in the former case. Because of this the nonlinear optical response of these species under action of nanosecond probe pulses was at the threshold of registration.

2.3. Third Harmonic Generation in the Laser-produced Ag NPs Plasmas

Figure 6 presents the spectra and the intensity of the third harmonic (TH) as a function of the probe and heating pulse intensity in the plasma plumes containing Ag NPs. One can see a six fold enhancement of TH efficiency in the case of silver plasma compared with the THG in air. Third harmonic yield was also analyzed at the air pressure of 1.3 kPa. In that case, the 20× enhancement of TH yield from Ag plasma with regard to residual air was obtained. A slope of fitting line in Fig. 6b corresponds to 3, which is the indication of the expected cubic dependence between fundamental and harmonic pulses in the case of THG. Figure 6c shows the dependence of TH yield on the heating pulse energy. Third harmonic generation did not show the saturation at the highest used energy of heating picosecond pulses (0.5 mJ).

A deviation from linear polarization led to a decrease of TH intensity, which is typical for low- and

Table 1. Nonlinear optical parameters of Ag NP suspensions. Reproduced from [32]. With permission of Springer

		Ag NPs (8 nm)	Ag NPs (50 nm)	Ag NPs (15 nm)
		Parameters of heating pulses		
		$\lambda = 1064$ nm, $\tau = 5$ ns, $E = 40$ mJ	$\lambda = 800$ nm, $\tau = 200$ ps, $E = 0.56$ μJ	$\lambda = 800$ nm, $\tau = 60$ fs, $P = 0.96$ μJ
800 nm, 60 fs	γ (cm^2 W^{-1})	2.0×10^{-15}	3.4×10^{-15}	1.9×10^{-15}
	β_{2PA} (cm W^{-1})	1.0×10^{-10}	0.9×10^{-10}	0.9×10^{-10}
	$\chi^{(3)}$ (esu units)	1.8×10^{-9}	2.6×10^{-9}	1.6×10^{-9}
400 nm, 60 fs	γ (cm^2 W^{-1})	2.1×10^{-15}	1.5×10^{-15}	3.2×10^{-15}
	β (cm W^{-1})	RSA: 8.6. $\times 10^{-10}$	RSA: 5.5×10^{-10}	2PA: 5.5×10^{-10}
	β_{SA} (cm W^{-1})	-1.9×10^{-10}	–	–
	$\chi^{(3)}$ (esu units)	3.6×10^{-9}	2.8×10^{-9}	3.3×10^{-9}
1064 nm, 5 ns	γ (cm^2 W^{-1})	-1.2×10^{-14}	–	–
	β_{2PA} (cm W^{-1})	3.0×10^{-10}	–	–
	$\chi^{(3)}$ (esu units)	0.6×10^{-9}	–	–
355 nm, 5 ns	γ (cm^2 W^{-1})	–	-2.5×10^{-15}	–
	β_{RSA} (cm W^{-1})	2.0×10^{-10}	9.0×10^{-10}	–
	β_{SA} (cm W^{-1})	-3.0×10^{-11}	–	–
	$\chi^{(3)}$ (esu units)	-0.2×10^{-9}	0.8×10^{-9}	–

high-order harmonics. The application of circularly polarized laser pulses led to complete disappearance of harmonic emission, as it should occur assuming the origin of the harmonic generation process.

The conversion towards 266 nm radiation in the case of plasma plume was notably stronger compared with THG in air. Third harmonic generation conversion efficiencies in air and Ag NP plasmas were determined to be 1×10^{-3} and 4×10^{-3} in the case of 800 nm, 60 fs driving pulses. The value of conversion efficiency in air was comparable with earlier reported studies carried out at similar conditions [35, 36]. Third harmonic enhancement in the Ag NP plasmas was attributed to involvement of small silver clusters in the harmonic generation.

3. ABLATED NICKEL NPs: THIRD HARMONIC GENERATION AND OPTICAL NONLINEARITIES

Another interesting and rarely studied topics is the formation of nickel NPs. Below we analyze the studies

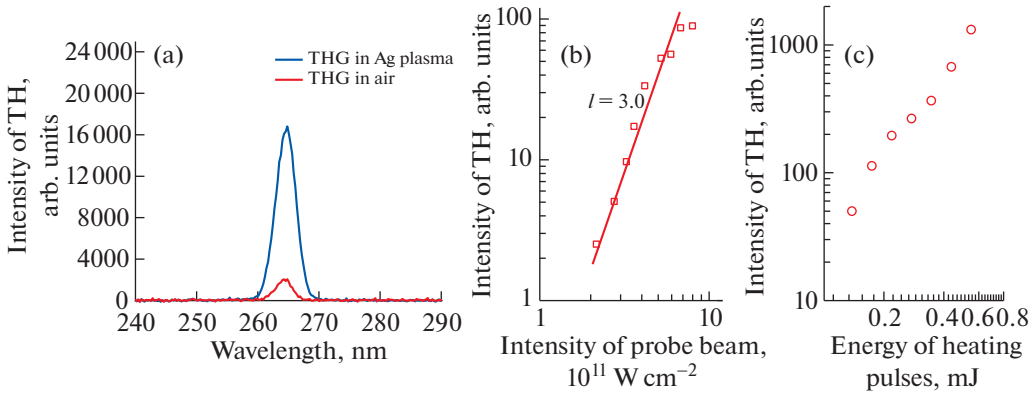

Fig. 6. (Color online) (a) Spectra of the third harmonic generation in the plasma containing Ag NPs (thick curve) and in the air (thin curve). (b) Dependence of the intensity of TH on the intensity of femtosecond laser pulses in silver plasma. (c) Dependence of the intensity of TH on the energy of heating picosecond laser pulses. Reproduced from [32]. With permission of Springer.

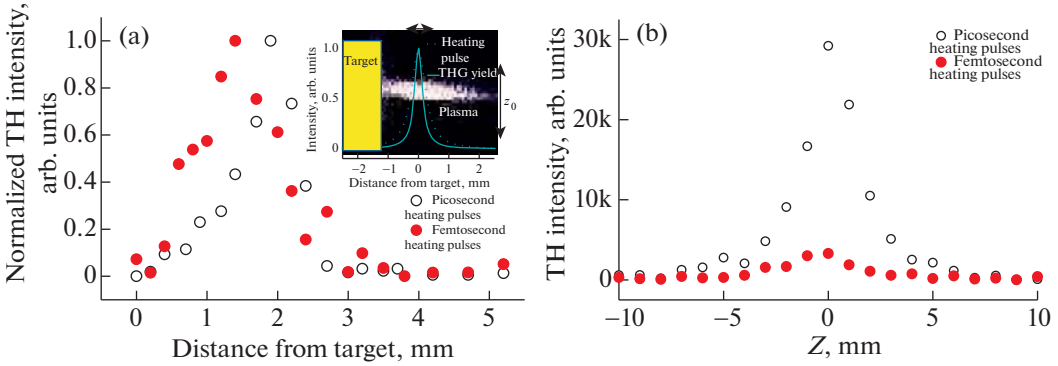

Fig. 7. (Color online) Variations of TH as the functions of (a) the distance between the target and the optical axis of the probe pulse at the constant heating pulse energies of 163 μJ (ps pulses, empty circles) and 48.5 μJ (fs pulses, filled circles) and (b) the position of the focal plane of probe pulse relative to the plasma at the constant heating pulse energies of 163 μJ (ps heating pulses, empty circles), 48.5 μJ (fs heating pulses, filled circles) and probe pulse energy of 30 μJ. Inset in Fig. (a) shows the scheme of TH variation vs. distance of the probe pulse with respect to the target. Reproduced from [37].

where formation of plasma from Ni target in air conditions was carried out using the 200 ps, while pulse width of the probe laser beam was kept at 60 fs [37]. Heating pulses reached the Ni target 38 ns before the probe pulses propagation. The generated TH radiation ($\lambda = 266$ nm) was separated from co-propagating fundamental beam using dichroic filter and registered by a fiber spectrometer (Ocean Optics). The target was moved with constant speed to achieve the stable TH yield.

The ablation of Ni was carried out in deionized water using 60 fs and 200 ps pulses. The 6 ns, 1064 nm pulses were also used for ablation of the Ni target immersed in liquid. Laser pulse energies of 51, 0.542, and 0.596 mJ were used for ns, ps and fs ablation. Each ablation experiment was performed during 30 min. From here onward, the prepared samples of Ni NPs suspensions are refereed as S_n, S_p, and S_f, respectively for ns, ps, and fs ablation processes.

The Ni NPs were characterized using SEM analysis. SEM images of Ni NPs show that the prepared NPs are spherical in shape. The mean size of NPs formed using fs laser pulse ablation was 50 nm which was smaller compared to Ni NPs prepared using ps laser ablation with the average particle size of 75 nm. This can be explained by the fact that two processes compete during ultrafast laser irradiation, which include columbic explosion and near-field enhancement at the surface of the NPs during ultrafast irradiation [38]. The columbic explosion is the dominant factor during femtosecond pulse irradiation compared to the picosecond laser irradiation where the effect of coulomb explosion decreases [39] and the near-field enhancement occurs due to the energy imbalance in the nanoparticle surface [40].

The mean size of Ni NPs in S_n was smaller compared to the cases of ablation by ps and fs pulses (S_p and S_f). During irradiation by ns pulses, the photo-thermal effect [41] becomes dominant compared to other processes of ablation causing the melting and evaporation at the surface of particle, which results in the temperature imbalance between the particle surface and bulk leading to the particle fragmentation. These processes can be further influenced by thermal conductivity and thermal expansion coefficient of the Ni during photo-thermal fragmentation at ns pulses ablation [42]. During ns ablation, the temperature growth on the surface of Ni is much faster compared to the case of thermal expansion of the molten Ni, which can lead to smaller sized particles formation.

3.1. Third Harmonic Generation in Ni NPs Plasma

A systematic study on the generation of the TH in the Ni plasma produced in air was performed using 800 nm probe pulses. The presence of Ni NPs in plasma was confirmed by analyzing the deposited materials from nearby substrates. In the first set of THG studies in plasmas, the 200 ps pulses were used as a heating radiation to create plasma. In the second case, both 60 fs heating and probe pulses were used.

Figure 7a shows the variation of TH intensity as a function of the distance between the target and the propagation axis of the probe pulse. Third harmonic from Ni plasma was observed up to the distance of 3 mm away from Ni target with maximum harmonic intensity at 1.9 and 1.4 mm for the ps and fs heating pulses, respectively. Third harmonic intensity variations were symmetric around the maximal position of TH. The profile around TH maximal intensities can be explained by the fact that the change of the focal position leads to change in the spot size in plasma. At the constant pulse energy, the plasma plume showed a stream-like shape at smaller spot size, whereas the plasma plume exhibited the hemispherical structure at larger spot size. Earlier studies have shown the effect of

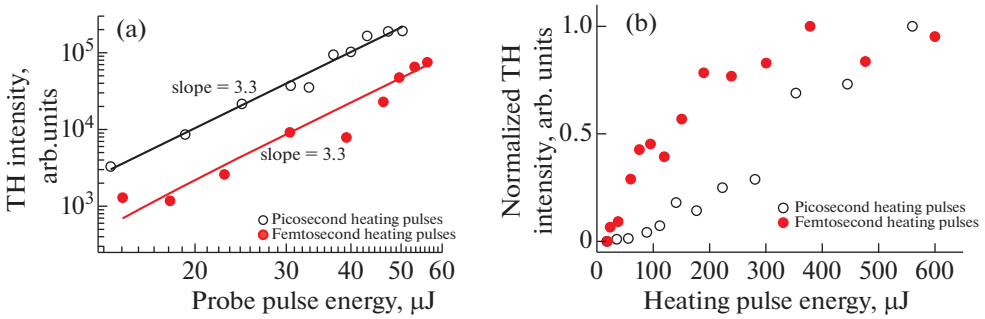

Fig. 8. (Color online) Variations of the TH in Ni plasma with (a) probe pulse energy at the constant heating energies of ps pulses (163 μJ, empty circles) and fs pulses (48.5 μJ, filled circle) and (b) heating energies of ps and fs pulses at the constant probe pulse energy of 30 μJ. Reproduced from [37]. © IOP Publishing. Reproduced with permission. All rights reserved.

spot size on the expansion of plasma. It has been demonstrated that the distribution of generated species during ablation is controlled by their longitudinal velocity, and strongly depends on input fluence [43]. The distribution of different species during ablation has direct influence on the TH intensity with the change of the probe focal position that resulted in the maximal TH intensity away from target surface. This behavior of TH signal from Ni plasma using ps and fs heating pulses points out the importance of plasma expansion velocity during pulsed laser ablation [44].

The inset in Fig. 7a depicts the TH intensity profile with varying spot size upon change of the focal plane of heating pulses. The spot size variation changes the fluence of heating pulses on the target surface during ablation, which eventually produces different concentration of plasma in the path of the probe beam. The image shows that there is a change in the intensity of the heating pulses at different positions of the target, which leads to the change of plasma concentration.

Figure 7b shows the dependence of the TH signal from the Ni plasma as a function of z position of the focused probe pulse at the pulse energy of 30 μJ. The energies of the ps and fs heating pulses were kept at 163 and 48.5 μJ, respectively. These measurements were performed by analyzing different plasma regions at the fixed distance of probe beam (1.9 mm in the case of ps heating pulses and 1.4 mm in the case of fs heating pulses) relative to the Ni target. The relative efficiency of THG using ps heating pulses was notably higher compared to the fs heating pulses.

The variations of the TH intensity with variation of pulse energy of the heating and probe pulses were analyzed under the optimal conditions for TH from Ni plasma. The energies used for the formation of plasma were fixed at 163 and 48.5 μJ for the ps and fs pulses, respectively. Figure 8a shows the TH yield from the Ni plasma increasing with the growth of the probe pulse energy. Variation of TH intensity shows approximately cubic dependence on the probe pulse energy up to ~50 μJ. At the constant probe pulse energy of 30 μJ, the TH intensity increases with the growth of heating pulse energy for both ps and fs heating pulses up to 600 μJ (Fig. 8b). Third harmonic monotonically increases with the increase of ps heating pulses energy, whereas for fs heating pulses, TH reaches saturation at the pulse energy of 200 μJ. The saturation can be caused by high concentration of free electrons in the Ni plasma produced by intense femtosecond heating pulses that lead to phase mismatch between the probe and TH waves.

3.2. Nonlinear Optical Properties of Ni NP Suspensions

The prepared Ni NPs suspensions were used to study their nonlinear optical properties by Z-scan technique at 800 and 400 nm. The OA Z-scan technique was employed to measure the 2PA coefficients. The results of studies are shown in Figs. 9a–9c for 800 nm, 60 fs pulses (empty circles) and summarized in Table 2. It was found that S_p possesses slightly larger 2PA ($\beta = 2.1 \times 10^{-11}$ cm W^{-1}) compared to that for S_n and S_f (both 1.5×10^{-11} cm W^{-1}). Nonlinear optical response of Ni NPs suspensions can be attributed to

Table 2. Nonlinear optical parameters of Ni NP suspensions prepared using laser ablation. Reproduced from [37]. © IOP Publishing. Reproduced with permission. All rights reserved

Wavelength, pulse duration	Sample	2PA coefficient (cm W^{-1})	Nonlinear refractive index (cm^2 W^{-1})
800 nm, 60 fs	S_n	1.5×10^{-11}	6.6×10^{-16}
	S_p	2.1×10^{-11}	5.4×10^{-16}
	S_f	1.5×10^{-11}	6.6×10^{-16}
400 nm, 60 fs	S_n	8.9×10^{-11}	2.1×10^{-15}
	S_p	4.2×10^{-11}	1.6×10^{-15}
	S_f	6.2×10^{-11}	1.4×10^{-15}

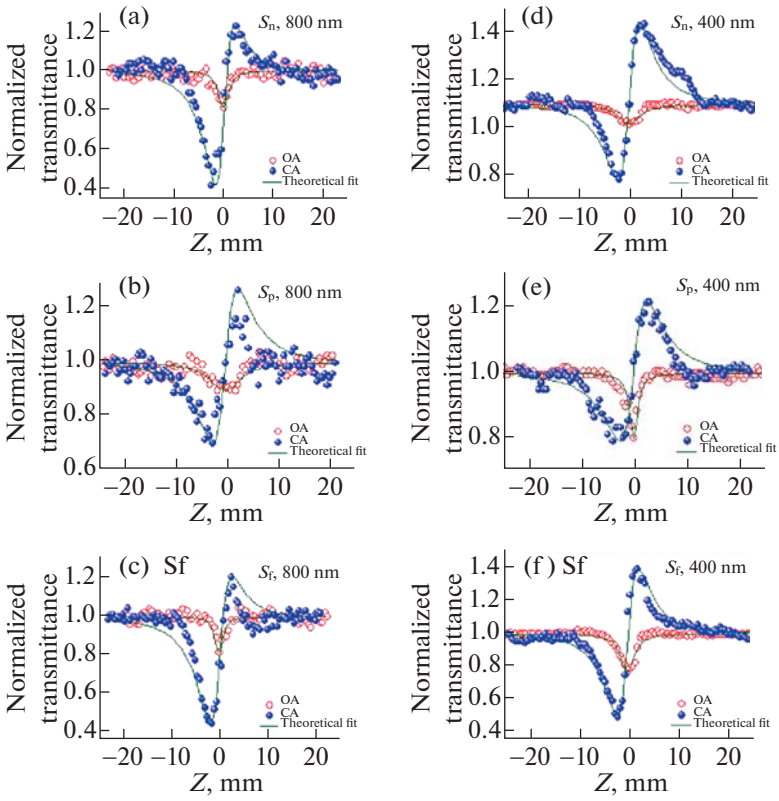

Fig. 9. (Color online) *Z*-scans of different Ni NPs in deionized water. (a), (b), and (c) represent the *Z*-scan traces of S_n, S_p, and S_f using 800 nm radiation. *Z*-scan traces of S_n, S_p, and S_f using 400 nm radiation are shown in (d), (e) and (f), respectively. Solid lines show the theoretical fits. Reproduced from [37]. © IOP Publishing. Reproduced with permission. All rights reserved.

the influence of particle size [45], which is larger for S_p as compared to the S_n and S_f.

It is worth to mention that 800 nm wavelength falls in the tail of absorption spectrum for all ablated NPs, which leads to low 2PA probability. Indeed, the steep growth of absorption appears in the UV region (≤330 nm) of the spectrum of Ni NPs suspensions. However, the absorption starts to gradually grow from 500 nm towards shorter wavelengths in the visible region. Low nonlinear absorption using 800 nm probe pulses was caused by low 2PA due to relatively small linear absorption at 400 nm for three suspensions. However, it was not negligible to entirely exclude the 2PA process. To analyze the probability of the influence of higher-order nonlinear optical process, like three-photon absorption (3PA), on the *Z*-scans of samples, the intensity-dependent studies of the nonlinear optical properties of these NPs suspensions were performed. During these studies, the β in all suspensions remained almost unchanged in the case of a two-fold growth of the probe pulse energy. Notice that 3PA characterizes by the relation $\beta \approx \beta_{2pa} + \beta_{3pa}I$, which shows the dependence of β on the probe pulse intensity *I*. It was concluded from these intensity-dependent studies that the role of 3PA was insignificant compared with 2PA.

The NLR indices of S_n, S_p, and S_f suspensions were also measured using femtosecond laser pulses (filled circles, Figs. 9a–9c). The nonlinear refraction at 800 nm shows the self-focusing properties at 1 kHz pulse repetition rate. This effect is related with Kerr-induced process rather than thermal processes since laser pulses are separated with the time of 1 ms, which is sufficient for dissipation of the absorbed energy from femtosecond laser pulses. The NLR indices were determined to be 6.6×10^{-16}, 5.4×10^{-16}, and 6.6×10^{-16} cm^2 W^{-1} for S_n, S_p and S_f, respectively. The calculated NLR indices showed the reverse trend compared to 2PA coefficients. The value of γ was lower for S_p compared to the other two samples. The NLR of all studied samples was related to the contribution of intense laser pulse induced electronic polarization.

Z-scans were also performed at λ = 400 nm to analyze the influence of SPR in Ni NPs on the nonlinear optical characteristics of these suspensions (Figs. 9d–9f). At 400 nm, all NPs suspensions possessed higher 2PA and self-focusing compared to the same processes measured using 800 nm pulses (see Table 2). The values of β were 9×10^{-11}, 4×10^{-11} and 6×10^{-11} cm W^{-1}

for S_n, S_p, and S_f, respectively. The study of NLR indices revealed the values of 2.1×10^{-15}, 1.6×10^{-15}, and 1.4×10^{-15} cm^2 W^{-1} for S_n, S_p, and S_f, respectively.

4. LASER ABLATION-INDUCED SYNTHESIS AND NONLINEAR OPTICAL CHARACTERIZATION OF TITANIUM AND COBALT NPs

4.1. Ablation and Characterization of Samples

The NPs were formed via laser ablation of the Ti and Co sheets immersed in a liquid-containing fused silica cell [46]. The incident light was focused on the 1-mm-thick metal sheet using a 100 mm focal length spherical lens, while the 20 mm thick cell was moved along two directions (X and Y) at a velocity of 0.01 mm s^{-1}. The ablation was performed using uncompressed radiation of Ti: sapphire laser (200 ps, 800 nm) at 1 kHz repetition rate during 20 to 30 min. The bulk targets were ablated at pulse energy 550 μJ in deionized water, toluene and EG.

Figures 10 and 11 show the SEM images and size distributions of the Ti and Co NPs ablated in water toluene and EG, respectively. The size distribution of Ti NPs in water, toluene and EG lies in between 20–250, 10–100 and 20–60 nm, and having corresponding to mean sizes are 125, 30, 40 nm, respectively, whereas, the size distribution of Co NPs synthesized in water was centered at 90 nm. It is important to analyze the processes that determine the morphology of synthesized NPs to control the mean diameter and size distribution of the resulting particles by changing the solvent and pulse energy. Particularly, the sizes of Ti and Co NPs synthesized in water were larger than those prepared in toluene and EG. The surface shape of spherical Ti and Co NPs in water was smooth. Water is a highly polar liquid, and the presence of oxygen leads to formation of the oxides of Ti and Co NPs during laser ablation.

4.2. Nonlinear Optical Properties of Ti NPs

Figure 12 shows the Z-scans of Ti NPs measured using 800 nm, 60 fs pulses, as well as the solid curves corresponding to theoretical fits of experimental data. Figures 12a–12c and 12d–12f show the OA and CA Z-scan data corresponding to the Ti NPs in water, toluene, and EG, respectively. Similar experiments were carried out in the case of 400 nm, 60 fs probe pulses. The nonlinear optical parameters of Ti NPs at 800 and 400 nm are comprised in Table 3. At the 800 nm probe wavelength, the Ti NPs in both water and toluene solutions showed the SA ($\beta = -2.1 \times 10^{-11}$ and $\beta = -2.3 \times 10^{-11}$ cm W^{-1}, respectively; Figs. 12a, 12b). In the case of CA the combined processes of NR and SA were observed in these suspensions that was manifested by larger peaks compared with preceding valleys (Figs. 12d, 12e). Meanwhile, the influence of SA in Ti

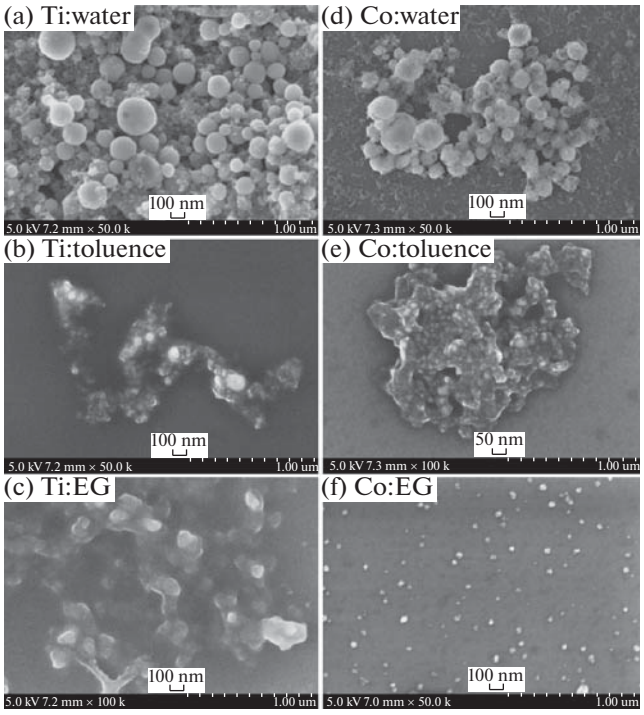

Fig. 10. SEM images of (a–c) Ti and (d–f) Co NPs ablated in deionized water, toluene and ethylene glycol solutions. Reproduced from [46]. With permission of Springer.

NPs in the case of ablation in EG was diminished due to high positive nonlinear absorption of pure solvent (Figs. 12c, 12f). The negative nonlinear absorption attributed to Ti NPs was smaller compared to the positive nonlinear absorption attributed to EG.

Overall, the Ti NPs suspended in EG showed the positive nonlinear absorption in the OA scheme. The corresponding nonlinear absorption coefficient in this suspension was $\beta = 7.2 \times 10^{-12}$ cm W^{-1}. In the case of CA scheme the Ti NPs in EG demonstrated pure self-focusing ($\gamma = 1.2 \times 10^{-15}$ cm^2 W^{-1}, Fig. 12f), whereas in water and toluene solutions these particles showed the NLR+SA processes ($\gamma = 5 \times 10^{-16}$ cm^2 W^{-1}, $I_{sat} = 3.9 \times 10^{11}$ W cm^{-2}, and $\gamma = 4.9 \times 10^{-16}$ cm^2 W^{-1}, $I_{sat} = 3.8 \times 10^{11}$ W cm^{-2}, respectively). These OA Z-scans demonstrated that the Ti NPs possess SA at 800 nm in case of 60 fs probe pulses. The values of nonlinear refraction and absorption coefficients of Ti NPs in water were slightly higher compared to Ti NPs in toluene. These studies showed that at relatively small intensities (7×10^{10} W cm^{-2}), SA is the prevailing process of nonlinear absorption that confirms the behavior of OL curve for Ti NPs suspension at small pulse energies (Fig. 12b). Then, with the growth of laser intensity, i.e., at $I_0 > 10^{11}$ W cm^{-2}, SA process became replaced by RSA leading to OL in this suspension.

In the case of 400 nm probe pulses the Ti NPs in three solvents showed stronger nonlinear absorption and refraction compared to 800 nm pulses due to close-

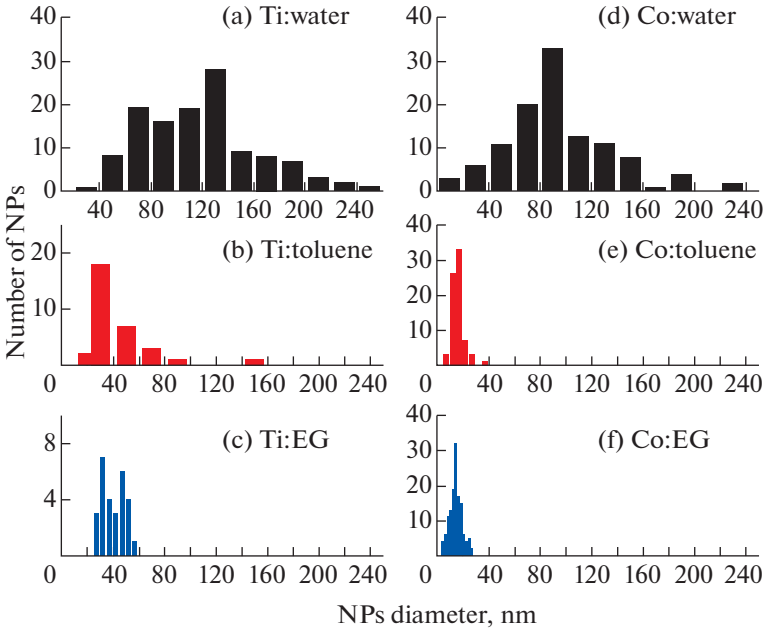

Fig. 11. (Color online) Histograms of size distribution of the Ti (a–c) and Co (b–d) NPs synthesized during ablation in deionized water, toluene and ethylene glycol solutions. Reproduced from [46]. With permission of Springer.

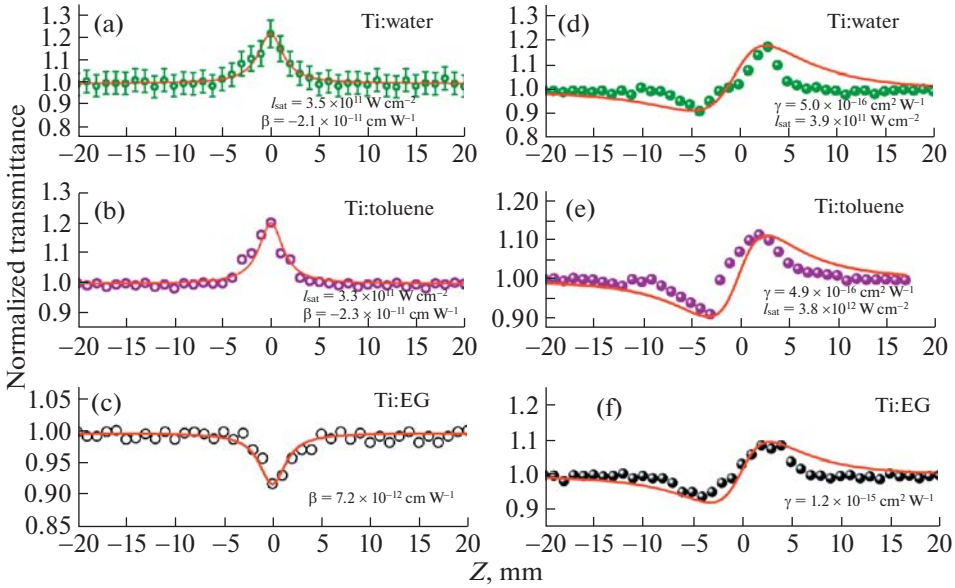

Fig. 12. (Color online) (a–c) OA, and (d–f) CA Z-scans of Ti NPs in different liquids measured using 800 nm radiation. The probe pulse intensities for each of these measurements are presented in Table 3. Reproduced from [46]. With permission of Springer.

ness of probe pulses to the SPR of Ti NPs. Ti NPs in water demonstrated the largest nonlinear absorption at $\lambda = 400$ nm compared to other two solvents. Both 2PA and RSA could be responsible for positive nonlinear absorption in these conditions. The nonlinear optical characteristics comprised in Table 1 show that the values of nonlinear absorption coefficients for the Ti NPs in these solvents followed the relation $\beta_{water} > \beta_{EG} > \beta_{toluene}$ at $\lambda = 400$ nm. In the meantime, the nonlinear refraction indices of Ti NPs suspensions did not follow this rule and were roughly equal to each other.

4.3. Nonlinear Optical Properties of Co NPs

Figure 13 shows the OA and CA *Z*-scans of the Co NPs ablated in water, toluene and EG in case of

Table 3. Nonlinear processes and parameters of Ti NP suspensions calculated using 800 and 400 nm, 60 fs radiation. Reproduced from [46]. With permission of Springer

NPs suspension	Nonlinear process in case of		I_0 (W cm^{-2}) × 10^{10}	γ (cm^2 W^{-1}) × 10^{-16} CA	β (cm W^{-1}) × 10^{-11}	I_{sat} (W cm^{-2}) × 10^{11}	
	OA	CA			OA	OA	CA
Measurements using 800 nm radiation							
Ti : water	SA	NR + SA	7.9	5	−2.1	3.5	3.9
Ti : toluene	SA	NR + SA	6.6	4.9	−2.3	3.3	3.8
Ti : EG	2PA	NRA	10	12	0.72		
Measurements using 400 nm radiation							
Ti: water	RSA	NRA	1.6	22	28		
Ti: toluene	RSA	NRA	1.6	32	7.8		
Ti: EG	RSA	NRA	1.6	26	8.8		

Table 4. Obtained nonlinear process from OA, CA *Z*-scans (800 nm, 400 nm) and their parameters of Co NPs in water, toluene and ethylene glycol. Reproduced from [46]. With permission of Springer

NPs suspension	Nonlinear process in case of		I_0 (W cm^{-2}) × 10^{11}	γ (cm^2 W^{-1}) × 10^{-16}	β (cm W^{-1}) × 10^{-12}
	OA	CA			
Measurements using 800 nm radiation					
Co : water	2PA	NRA	2.7	1.5	8
Co : toluene	2PA	NRA	2.5	4.8	15
Co : EG	2PA	NRA	2.2	3.8	6
Measurements using 400 nm radiation					
Co : water	RSA	NRA	2.2	1.6	5.0
Co : toluene	RSA	NRA	0.3	7.3	110
Co : EG	RSA	NRA	0.5	21	210

800 nm probe pulses, respectively. Similar measurements were performed using 400 nm probe pulses. The corresponding nonlinear optical processes and their parameters are comprised in Table 4. In the case of OA *Z*-scans the Co NPs in water, toluene and EG demonstrated the 2PA or RSA (800 nm) and RSA (400 nm), whereas CA scheme revealed the nonlinear refraction and absorption. The values of γ and β for Co NPs in toluene ($I_0 = 2.5 \times 10^{11}$ W cm^{-2}) were slightly higher than those for Co NPs in water ($I_0 = 2.7 \times 10^{11}$ W cm^{-2}) and EG ($I_0 = 2.2 \times 10^{11}$ W cm^{-2}). It was expected to be high values of γ and β for Co NPs in EG, due to their small size of distribution. The nonlinear absorption studies of Co NP suspensions showed that this process was observed at both wavelengths (800 nm and 400 nm).

The absorption peak of Co NPs in water demonstrates the SPR at 400 nm. These NPs have stronger linear absorption at 400 nm compared to 800 nm. At both 800 and 400 nm wavelengths the Co NPs in three solvents have shown the nonlinear refraction and absorption indicating the self-focusing condition while using short (60 fs) pulses. The nonlinear optical parameters of Co NPs in water have higher values at 800 nm compared to 400 nm. However, the smallest NPs (in case of toluene (SPR peak at 287 nm) and EG (SPR peak at 310 nm)) have strong nonlinear absorption and refraction coefficients at resonance wavelength (400 nm). The highest values of β (2.1×10^{-10} cm W^{-1}) and γ (2.1×10^{-15} cm^2 W^{-1}) are achieved for Co NPs in EG.

5. SUMMARY

The selection of the topics of this review follows with some logical sequences. Optical limiting effect is a process caused by the nonlinear optical properties of materials. It can be explained by *Z*-scan data. It was demonstrated, through harmonic generation, that ablation and formation of NPs in liquids and air has the advantages, which can be used for HHG in the laser-produced plasmas containing NPs and quantum dots. Furthermore, the increase of TH yield in the plasmas containing NPs allows basic explanation of the formation of these NPs at different conditions. These groups of studies were analyzed to demonstrate the fact that exceptionally strong nonlinearities (par-

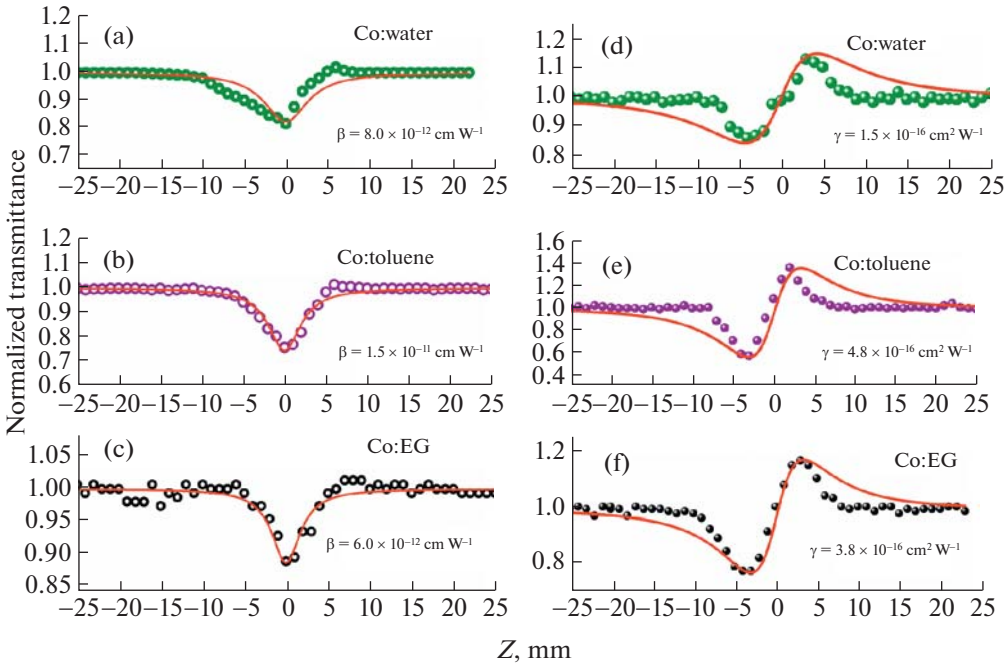

Fig. 13. (Color online) (a, b, c) OA, and (d, e, f) CA Z-scans (800 nm, 60 fs) of the Co NPs obtained during ablation in water (a, d), toluene (b, e), and (c, f) ethylene glycol, respectively. The corresponding nonlinear optical parameters are shown on the graphs. Reproduced from [46]. With permission of Springer.

ticularly, nonlinear absorption) strongly correlate with highly efficient THG in NPs. The reviewed studies show the way to attribute the earlier reported exceptionally strong HHG conversion efficiency in NP plasmas to the specific features of those particles related with involvement of their plasmonic properties in the enhancement of nonlinear optical response in the XUV range.

In this review, we have analyzed the results of studies of the Ag NPs prepared during ablation of bulk silver in deionized water using different wavelengths and durations of heating pulses. The study of the nonlinear optical parameters of Ag NPs in the resonant and quasi-resonant conditions using 400 nm, 60 fs pulses have shown the presence of SA and RSA. The nonlinear absorption coefficient of suspensions was as high as 3.0×10^{-5} cm W^{-1} at the wavelength of 1064 nm. The Ag NP suspension has demonstrated the outstanding optical limiting properties in the case of 355 nm, 5 ns probe pulses. Nonlinear refraction showed the change of sign with variation of the wavelength and duration of laser pulses.

The application of small-sized NPs for low-order harmonic generation of femtosecond laser pulses was demonstrated and systematically analyzed during ablation of silver in air. The enhancement of low-order harmonic generation is attributed to the influence of silver clusters on the nonlinear optical response of Ag plasma. Those studies have demonstrated the involvement of multi-atomic Ag particles in the growth of third harmonic yield. The conversion towards 266 nm radiation in the case of plasma plume was notably stronger compared with THG in air.

Further, we have analyzed the nonlinear optical response of nickel NPs prepared using nanosecond, picosecond, and femtosecond pulse induced ablation in deionized water, as well as discussed the studies of the lower-order harmonic generation in the plasma containing these NPs. The influence of NP size distribution on the nonlinear optical properties was observed at 800 nm with the maximum two-photon absorption coefficient of 2×10^{-11} cm W^{-1} for nickel NPs suspensions prepared using picosecond laser pulses. The larger two-photon absorption coefficient of (9×10^{-11} cm W^{-1}) was measured for nickel NPs suspension at 400 nm, which was attributed to the influence of surface plasmon resonance. Similar to two-photon absorption coefficients, nonlinear refraction have shown larger indices at 400 nm as compared to the 800 nm.

Finally, titanium and cobalt NPs were synthesized using laser ablation technique in different liquid solvents (water, toluene, and ethylene glycol) were systematically analyzed. The third-order nonlinear optical properties of these NPs were studied using the 60 fs pulses at two wavelengths. Ti and Co NPs showed SA and 2PA at 800 nm and RSA at 400 nm. At 800 nm in the case of CA Z-scans the joint influence of nonlinear refraction and SA was observed for Ti NPs in water and toluene, whereas nonlinear refraction and positive absorption were dominated in the ethylene glycol solution containing these NPs. The Ti and Co NPs

showed positive nonlinear refraction at both 800 and 400 nm. The Ti NPs ablated in water demonstrated the SA in the case of 355 nm, 5 ns pulses at lower energies and RSA at larger energies. The measurements of *Z*-scans and optical limiting demonstrated that the Ti NPs have higher nonlinear absorption and refraction coefficients as compared to Co NPs.

REFERENCES

1. S. Porel, N. Venkatram, D. Narayana Rao, and T. P. Radhakrishnan, J. Appl. Phys. **102**, 033107 (2007).
2. O. Muller, S. Dengler, G. Ritt, and B. Eberle, Appl. Opt. **52**, 139 (2013).
3. R. A. Ganeev, A. I. Ryasnyansky, A. L. Stepanov, M. K. Kodirov, and T. Usmanov, Opt. Spectrosc. **95**, 967 (2003).
4. R. A. Ganeev, M. Morita, A. I. Ryasnyansky, M. Baba, D. Rau, H. Fujii, M. Suzuki, M. Turu, and H. Kuroda, Opt. Spectrosc. **97**, 530 (2004).
5. J. P. Huang and K. W. Yu, Appl. Phys. Lett. **86**, 041905 (2005).
6. P. Baraskar, R. Chouhan, A. Agrawal, R. J. Choudhary, P. K. Sen, and P. Sen, Phys. Lett. A **382**, 860 (2018).
7. X. Mou, Z. Ali, S. Li, and N. He, J. Nanosci. Nanotech. **15**, 54 (2015).
8. S. Link, C. Burda, B. Nikoobakht, and M. A. El-Sayed, J. Phys. Chem. B **104**, 6152 (2000).
9. R. A. Ganeev, M. Baba, A. I. Ryasnyansky, M. Suzuki, and H. Kuroda, Appl. Phys. B **80**, 595 (2005).
10. R. A. Ganeev, M. Baba, A. I. Ryasnyansky, M. Suzuki, and H. Kuroda, Opt. Spectrosc. **99**, 668 (2005).
11. I. A. Sukhov, G. A. Shafeev, V. V. Voronov, M. Sygletou, E. Stratakis, and C. Fotakis, Appl. Surf. Sci. **302**, 79 (2014).
12. A. A. Serkov, P. G. Kuzmin, and G. A. Shafeev, Chem. Phys. Lett. **647**, 68 (2016).
13. M. Ali, N. Remalli, F. Yehya, A. K. Chaudhary, and V. V. S. S. Srikanth, Appl. Surf. Sci. **357**, 1601 (2015).
14. R. A. Ganeev, A. I. Ryasnyansky, and H. Kuroda, Opt. Spectrosc. **99**, 1006 (2005).
15. A. A. Serkov, E. V. Barmina, P. G. Kuzmin, and G. A. Shafeev, Chem. Phys. Lett. **623**, 93 (2015).
16. T. Tsuji, K. Iryo, N. Watanabe, and M. Tsuji, Appl. Surf. Sci. **202**, 80 (2002).
17. J. B. Han, D. J. Chen, S. Ding, H. J. Zhou, Y. B. Han, G. G. Xiong, and Q. Q. Wang, J. Appl. Phys. **99**, 1 (2006).
18. Y. Jiang, Y. Ma, Z. Fan, P. Wang, X. Li, Y. Wang, and Yu Zhang, Opt. Lett. **43**, 2 (2018).
19. R. A. Ganeev, A. I. Ryasnyansky, A. L. Stepanov, and T. Usmanov, Phys. Status Solidi B **241**, 935 (2004).
20. P. Baraskar, R. Chouhan, A. Agrawal, R. J. Choudhary, P. K. Sen, and P. Sen, Phys. Lett. A **382**, 860 (2018).
21. T. Hinotsu, B. Jeyadevan, C. N. Chinnasamy, K. Shinoda, and K. Tohji, J. Appl. Phys. **95**, 7477 (2004).
22. V. Amendola and M. Meneghetti, Phys. Chem. Chem. Phys. **11**, 3805 (2009).
23. J. K. Anthony, H. C. Kim, H. W. Lee, S. K. Mahapatra, H. M. Lee, C. K. Kim, K. Kim, H. Lim, and F. Rotermund, Opt. Express **16**, 11193 (2008).
24. H. Lu and W. Wang, Appl. Opt. **56**, 4690 (2017).
25. S. Amoruso, R. Bruzzese, X. Wang, N. Nedialkov, and P. A. Atanasov, J. Phys. D: Appl. Phys. **40**, 331 (2007).
26. D. M. Arboleda, J. M. J. Santillan, L. J. Mendoza Herrera, M. B. Fernandez van Raap, P. M. Zelis, D. Muraca, D. C. Schinca, and L. B. Scaffardi, J. Phys. Chem. C **119**, 13184 (2015).
27. S. Alikhani, H. Tajalli, and E. Koushki, Opt. Commun. **286**, 318 (2013).
28. Y. Ogata, A. Vorobyev, and C. Guo, Materials **11**, 501 (2018).
29. M. López-Arias, M. Oujja, M. Sanz, R. A. Ganeev, G. S. Boltaev, N. K. Satlikov, R. I. Tugushev, T. Usmanov, and M. Castillejo, J. Appl. Phys. **111**, 043111 (2012).
30. R. A. Ganeev, Opt. Spectrosc. **123**, 351 (2017).
31. R. A. Ganeev, L. B. Elouga Bom, and T. Ozaki, Opt. Spectrosc. **108**, 970 (2010).
32. G. S. Boltaev, R. A. Ganeev, P. S. Krishnendu, S. K. Maurya, P. V. Redkin, K. S. Rao, K. Zhang, and C. Guo, Appl. Phys. A **124**, 766 (2018).
33. N. Faraji, W. M. M. Yunus, A. Kharazmi, E. Saion, M. Shahmiri, and N. Tamchek, J. Eur. Opt. Soc. Rap. Public. **7**, 12040 (2012).
34. R. A. Ganeev, A. I. Ryasnyansky, S. R. Kamalov, M. K. Kodirov, and T. Usmanov, J. Phys. D **34**, 1602 (2001).
35. M. L. Naudeau, R. J. Law, T. S. Luk, T. R. Nelson, S. M. Cameron, and J. V. Rudd, Opt. Express **14**, 6194 (2006).
36. R. A. Ganeev, H. Singhal, P. A. Naik, J. A. Chakera, M. Kumar, and P. D. Gupta, Phys. Rev. A **82**, 043812 (2010).
37. K. Zhang, S. K. Maurya, R. A. Ganeev, K. S. Rao, and C. Guo, J. Opt. **20**, 125502 (2018).
38. J.-W. Jeon, S. Yoon, H. W. Choi, J. Kim, D. Farson, and S.-H. Cho, Appl. Sci. **8**, 112 (2018).
39. D. Werner, A. Furube, T. Okamoto, and S. Hashimoto, J. Phys. Chem. C **115**, 8503 (2011).
40. A. Plech, V. Kotaidis, M. Lorenc, and J. Boneberg, Nat. Phys. **2**, 44 (2006).
41. M. Kawasaki and N. Nishimura, Appl. Surf. Sci. **253**, 2208 (2006).
42. L. Abadlia, F. Gasser, K. Khalouk, M. Mayoufi, and J. G. Gasser, Rev. Sci. Instrum. **85**, 095121 (2014).
43. X. Li, W. Wei, J. Wu, S. Jia, and A. Qiu, J. Appl. Phys. **113**, 243304 (2013).
44. F. Claeyssens, M. N. R. Ashfold, E. Sofoulakis, C. G. Ristoscu, D. Anglos, and C. Fotakis, J. Appl. Phys. **91**, 6162 (2002).
45. P. C. Ray, Chem. Rev. **110**, 5332 (2010).
46. K. S. Rao, R. A. Ganeev, K. Zhang, Y. Fu, G. S. Boltaev, P. S. Krishnendu, P. V. Redkin, and C. Guo, J. Nanopart. Res. **20**, 285 (2018).